AGU PUBLICATIONS

Geophysical Research Letters

RESEARCH LETTER
10.1002/2015GL063494

Key Points:
- Rapid restratification of upper ocean following a storm close to an ocean front
- Development of near-inertial shear deviates from beta dispersion paradigm

Correspondence to:
A. Forryan,
af1c10@soton.ac.uk

Citation:
Forryan, A., A. C. Naveira Garabato, K. L. Polzin, and S. Waterman (2015), Rapid injection of near-inertial shear into the stratified upper ocean at an Antarctic Circumpolar Current front, *Geophys. Res. Lett.*, *42*, 3431–3441, doi:10.1002/2015GL063494.

Received 13 FEB 2015
Accepted 7 APR 2015
Accepted article online 11 APR 2015
Published online 7 MAY 2015

Rapid injection of near-inertial shear into the stratified upper ocean at an Antarctic Circumpolar Current front

Alexander Forryan[1], Alberto C. Naveira Garabato[1], Kurt L. Polzin[2], and Stephanie Waterman[1,3,4]

[1]University of Southampton, National Oceanography Center, Southampton, UK, [2]Woods Hole Oceanographic Institution, Woods Hole, Massachusetts, USA, [3]Climate Change Research Centre and ARC Centre of Excellence for Climate System Science, University of New South Wales, Sydney, New South Wales, Australia, [4]Department of Earth, Ocean and Atmospheric Sciences, University of British Columbia, Vancouver, British Columbia, Canada

Abstract The impact on the upper ocean of the passage of a short, intense storm over a Southern Ocean site, in proximity to an Antarctic Circumpolar Current front, is characterized. The storm causes a wind-induced deepening of the mixed layer and generates an inertial current. Immediate poststorm observations indicate a mixed layer extending to approximately 50 m depth. Subsequent measurements show the upper ocean to have restratified, injecting near-inertial shear in stratified waters within 1 day of the storm's passage. This time scale for the development of near-inertial shear is 1 order of magnitude shorter than that predicted by the β dispersion paradigm. The observed rapid changes in upper ocean stratification point to the existence of an as yet undocumented, efficient mechanism for injection of near-inertial shear into the stratified ocean that is in turn associated with enhanced turbulence and mixing.

1. Introduction

The action of the wind on the sea surface transfers kinetic energy and is a significant contributor to the dynamics of the ocean surface boundary layer [*Large et al.*, 1994]. This boundary layer is generally considered to compose of a well-mixed, near-boundary region and a thinner "transition layer" [*D'Asaro*, 1985; *Price et al.*, 1986; *Large et al.*, 1994]. The mixed layer is maintained by vigorous turbulent mixing that results in nearly homogeneous physical properties and nearly neutral stratification, though stratification and shear can have a short-term existence in the mixed layer until eroded by turbulent mixing [*Large et al.*, 1994]. The thinner transition layer separates the mixed layer from the ocean interior, is characterized by large gradients in physical properties, and is typically the site of maxima in shear and stratification [*Johnston and Rudnick*, 2009; *Sun et al.*, 2013].

Observations of wind acting on the surface ocean are often interpreted within the context of simple one-dimensional boundary layer models, such as the much used "slab" model [*Pollard and Millard*, 1970]. In these models, kinetic energy enters the ocean through a viscous stress applied over a single depth scale, typically either a prescribed mixed layer depth [*D'Asaro*, 1985; *Price et al.*, 1986; *Pollard and Millard*, 1970] or a boundary layer depth diagnosed using a bulk Richardson number criterion [*Large et al.*, 1994]. Where the depth of the boundary layer is not fixed as a model parameter, in the absence of ocean surface cooling, the process of boundary layer deepening is through shear from wind-generated surface currents entraining the deeper waters [*Price et al.*, 1986; *Large et al.*, 1994].

The kinetic energy that manages to escape from the upper ocean plays a significant role in the maintenance of the ocean's general circulation [*Wunch and Ferrari*, 2004; *Ferrari and Wunch*, 2009]. Kinetic energy is believed to propagate into the ocean interior through "inertial pumping," in which localized horizontal convergences and divergences associated with upper ocean inertial currents create a vertical velocity perturbation that generates pressure gradients and near-inertial internal waves in the stratified interior [*Gill*, 1984]. The rate of inertial pumping is considered to be determined by variations in the local planetary rotation rate (β), modulated by local gradients of relative vorticity, which causes a reduction in the spatial scales of inertial motion [*D'Asaro*, 1989; *Danioux et al.*, 2008, 2011]. In this β dispersion paradigm, the leakage of near-inertial kinetic energy into the stratified interior as near-inertial internal waves is a function of the time required to build up horizontal variations in mixed layer velocity: at small times, a characteristic horizontal wave number (ℓ) develops from the initial horizontal wave number of the wind forcing (ℓ_0) as $\ell = \ell_0 - \beta t$ [*D'Asaro*, 1989]. A linear dispersion relation is used to link this horizontal wave number to

vertical wave number with the unavoidable consequence that the accumulation of horizontal gradients in mixed layer velocity occurring over a time period of days to weeks must precede the emergence of small vertical-scale internal waves [*D'Asaro*, 1989].

In this article, we document the response of the upper ocean to the passage of a short but intense storm in proximity to an Antarctic Circumpolar Current (ACC) front in the Southern Ocean. We show that, as expected from one-dimensional boundary layer models, turbulent mixing initially intensifies, the surface mixed layer deepens, and an inertial current is generated. However, rapid changes in upper ocean stratification ensue and near-inertial shear is observable in stratified waters within approximately 1 day of the storm's passage. This time scale for the development of near-inertial shear is 1 order of magnitude shorter than that predicted by the β dispersion paradigm. The physical mechanisms underpinning the observed rapid changes in upper ocean stratification are explored within the context of the available observations.

2. Methods

During the RRS *James Cook* cruise JC29 to the Kerguelen Plateau (approximately 46°S, 72°E) in October–December 2008 as part of the SOFine project, opportunity arose to conduct a series of measurements during a storm that lasted for approximately 12 h from the morning of 13 November 2008 [*Naveira Garabato*, 2009]. The site of the measurements was in close proximity to an ACC front south of the main frontal jet (Figure 1). Measurements continued to be made in the same location until the early morning of 16 November 2008 (year day 321). The measurements consisted of a combination of microstructure velocity shear and conductivity-temperature-depth (CTD) stations. Measurements of wind speed, wind direction, and surface ocean currents were made continuously throughout the cruise via shipboard sensors. Using a Gill Windsonic ultrasonic wind sensor, 10 m wind speed and direction were measured. The raw 1 s wind data were despiked over a 10 min window by removing values greater than two standard deviations from the mean before being corrected for ship speed and orientation to produce absolute wind speed and direction [*Naveira Garabato*, 2009].

Current velocities were measured using a ship-mounted 150 kHz RD Instruments Ocean Surveyor acoustic Doppler current profiler (ADCP), with a vertical range of ~300 m, configured with 60 bins of 8 m height starting from a depth of 23.5 m. Calibration was carried out over a continental shelf en route to the survey site. All continuous measurements were averaged into 30 min intervals. Inertial currents were extracted from the raw ADCP data using a band-pass frequency domain filter consisting of a $\sin^2$ window of width $\approx 1.7 \times 10^{-5}$ Hz centered on the local inertial frequency (1.688×10^{-5} Hz at 46.6°S latitude; see Appendix A).

Turbulent kinetic energy dissipation was estimated directly from measurements of microstructure velocity shear made using an MSS90L microstructure profiler produced by Sea and Sun Technology GmbH and ISS Wassermesstechnik. The MSS90L is a lightly tethered free-fall profiler used for rapid repeat profiling in the surface (200 m depth) waters. The MSS90L was deployed on two stations, stations 7 and 11, which consisted of eight and six individual casts, respectively, taken over the course of approximately 1 h.

Assuming isotropic turbulence [*Yamazaki and Osborn*, 1990], the rate of turbulent kinetic energy dissipation (ε) can be calculated from the variance of the measured vertical microstructure shear by integration of the vertical microstructure shear power spectrum $\Phi(k)$ as

$$\varepsilon = \frac{15}{2}\nu \int_{k_l}^{k_c} \Phi(k)\, \mathrm{d}k$$

[*Moum et al.*, 1995; *Rippeth et al.*, 2003; *Stips*, 2005], where k is the vertical wave number, the limits of integration (k_c and k_l) are the Kolmogorov wave number and 1, respectively, and ν is the molecular viscosity of seawater. The microstructure shear power spectrum was estimated from the vertical microstructure shear fluctuations using the Welch-modified periodogram method [*Welch*, 1967]. This calculated power spectrum was then used to scale and dimensionalize a nondimensional analytical form of the empirical Naysmith universal turbulence power spectrum [*Roget et al.*, 2006], and the rate of turbulent kinetic energy dissipation calculated by integration of the fitted universal spectrum up to the Kolmogorov wave number. Instrument-specific corrections for shear probe attenuation were applied [*Prandke*, 2007].

Dissipation measurements made using the MSS90L microstructure profiler were corrected for the influence of the ship, which is assumed to extend to a depth of ~15 m (≈ 3× the vessel draft), by excluding all measurements for depths shallower than 15 m.

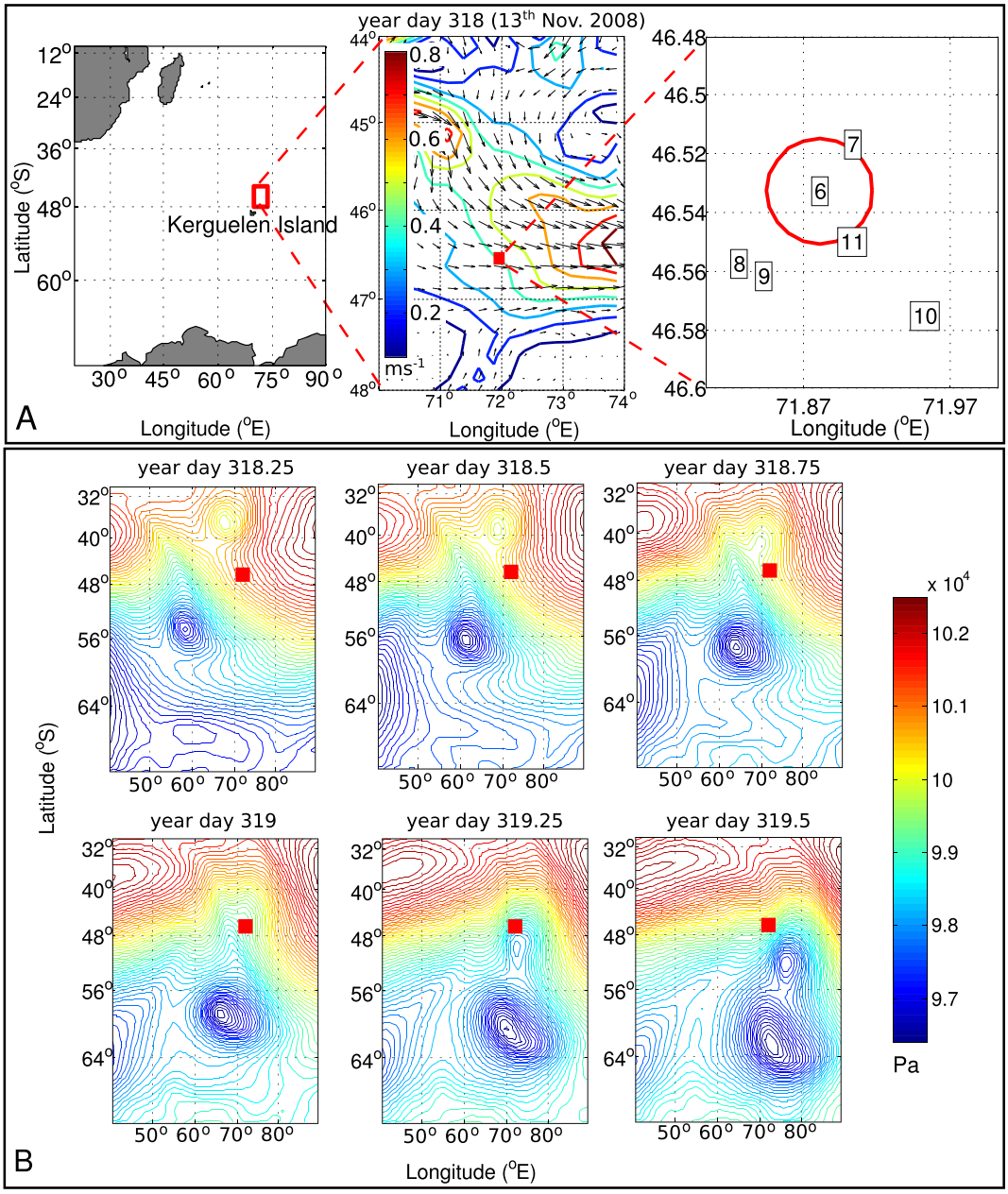

Figure 1. (a) Overview of the area where (left) observations were made. (middle) Contours of geostrophic sea surface speed (m s^{-1}), estimated from post-2014 Archiving, Validation, and Interpretation of Satellite Oceanographic data (AVISO) sea surface height data (arrows indicate direction) produced by Segment Sol multimissions d'ALTimétrie, d'Orbitographie/Developing Use of Altimetry for Climate Studies and distributed by AVISO, with support from Centre National d'Etudes Spatiales (http://www.aviso.altimetry.fr/duacs/). The red square marks the location of the observations; (right) individual station positions are shown, where the solid red circle indicates the mixed layer Rossby radius (2 km) for a mixed layer of 50 m depth centered on station 6. (b) A sequence of contours of sea level pressure at 1×10^3 Pa intervals taken from ERA-Interim mean sea level pressure data (0.75° × 0.75° resolution) for the period of the storm. The red square marks the location of the observations.

3. Results

During the period of the observations (year days 318–321) geostrophic sea surface velocity calculated from AVISO altimetric data indicates that the ACC was flowing almost due east (bearing 98°, Figure 1a) with speed ≈ 0.4 m s^{-1}, consistent with estimates made using ADCP measurements. ERA-Interim reanalysis data [*Dee et al.*, 2011] for the time of the storm (year days 318.2–318.5) show that the observed strong winds

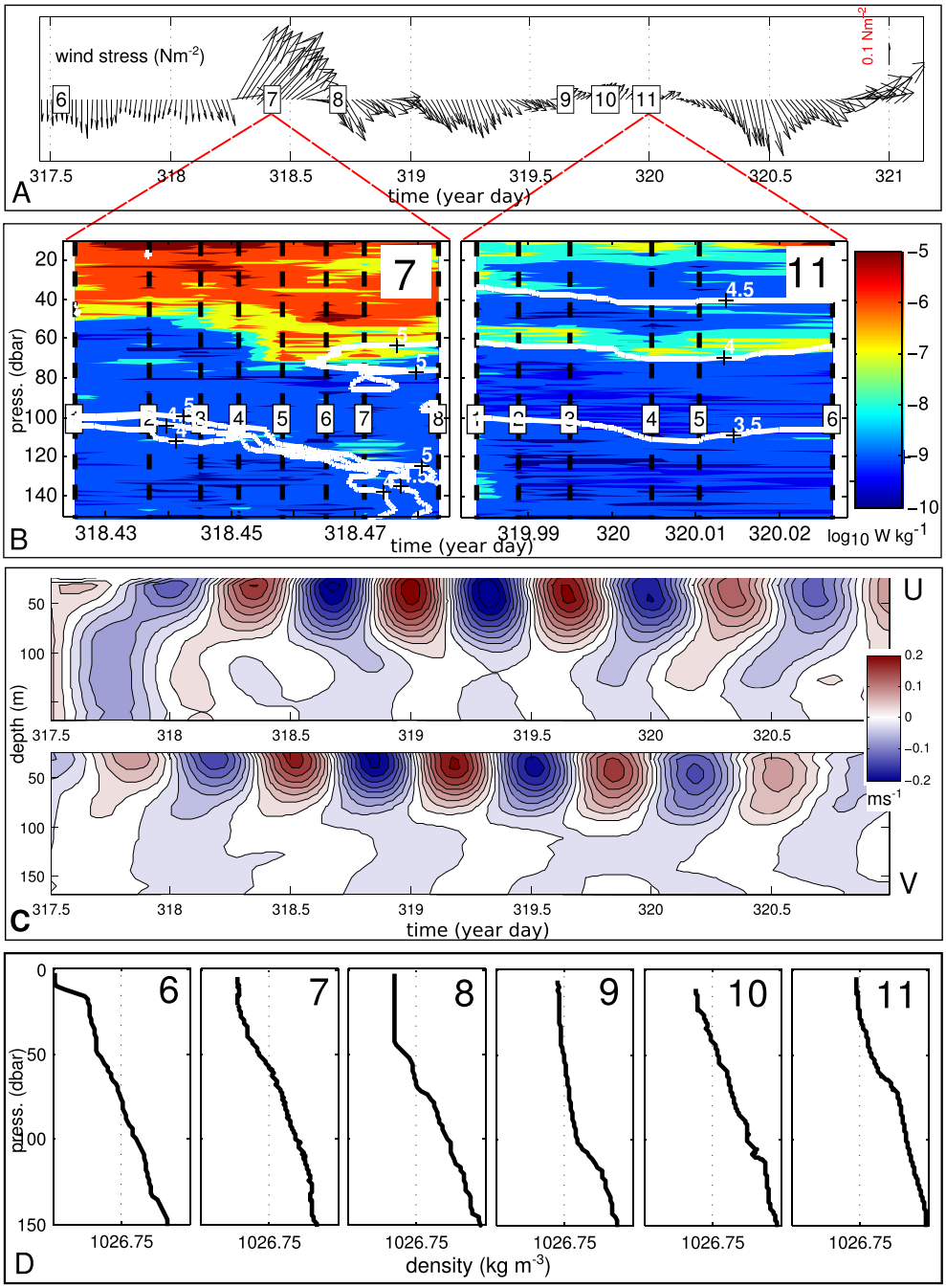

Figure 2. (a) Wind stress magnitude (N m^{-2}) and direction; times of the stations are indicated. (b) Contours of $\log_{10}$ turbulent kinetic energy dissipation (ϵ W kg^{-1}) for stations 7 and 11. The time of each microstructure profile is indicated by a numbered dashed black line. Contours of temperature in 0.5°C intervals from 3 to 5°C are shown in white. (c) Contours of inertial current velocity (*U* and *V* components, m s^{-1}) estimated by band-pass filtering the 150 kHz ADCP data. Contour intervals are 0.025 m s^{-1}. (d) Density profiles (kg m^{-3}) of the individual stations for the surface 150 m.

were likely to have been associated with a relatively small scale (compared to typical atmospheric features) atmospheric vortex merger (Figure 1b).

Prior to the storm (year day 318.2), the wind was blowing approximately due south (a cross-front direction). During the storm the wind direction rotated anticlockwise to blow approximately north-east (a cross-front/down-front direction, approximately 45° to the front). Immediately after the storm (year day 318.7), the wind direction rotated clockwise back to approximately due south. This pattern of the wind direction switching

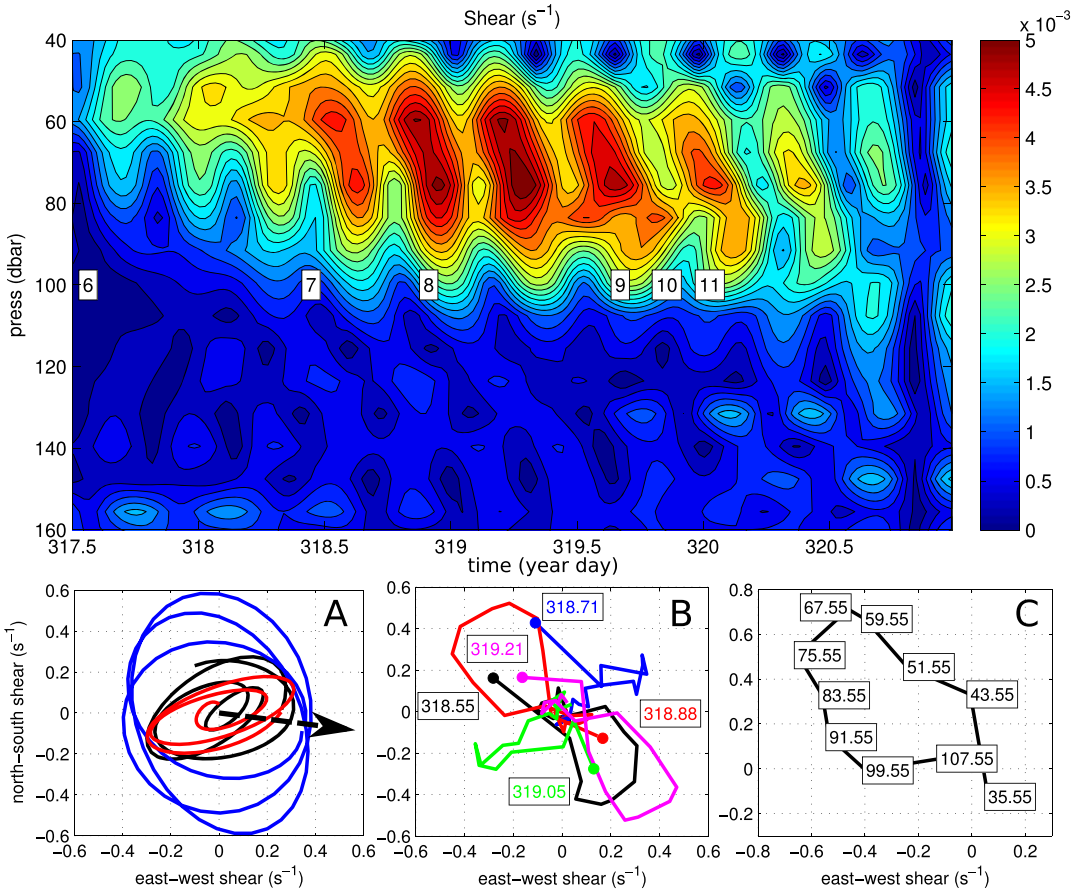

Figure 3. (top) Vertical shear magnitude (s^{-1}) calculated from the inertial current component in the 150 kHz ADCP data. The times of the stations are indicated. (a) Hodographs of the shear vector ($s^{-1} \times 10^2$) calculated over a depth interval of 8 m centered at three depth levels (31 m in black, 55 m in blue, and 95 m in red) for all times from year day 318 to year day 320. The dashed arrow indicates the direction of the barotropic surface current (magnitude 0.4 m s^{-1}) estimated from the time average of the ADCP data for the whole record. (b) Five depth profiles (from 27.5 m to 163.5 m) of inertial shear ($s^{-1} \times 10^2$). Each of the five profiles depicts the evolution of the vertical structure over one complete inertial period. The start of each profile is marked, and the time of each profile is labeled. (c) Subinertial shear time-averaged over ~ 1.5 inertial periods ($s^{-1} \times 10^3$) from the start of station 8 to the end of station 9. The measurement depths are indicated.

from due south to north-east (cross front to cross front/down front) was then repeated approximately every 24 h during the remainder of the observation period (Figure 2a).

Station 6 (prestorm) shows a clear surface mixed layer of ≈ 11 m depth, calculated using the method of *Kara et al.* [2000]. No surface mixed layer is apparent midstorm (station 7). However, the depth of this surface mixed layer increases to ≈ 48 m for station 8 at approximately the end of the storm. Station 9 shows the surface mixed layer partially restratified. Upper ocean stratification increases further through station 10 up to station 11, in which there is little or no indication of a surface mixed layer (Figure 2d).

During the storm, station 7, dissipation is initially elevated ($> 10^{-7}$ W kg^{-1}) above ocean background ($\approx 10^{-9}$ W kg^{-1}) down to approximately 40 m (Figure 2b). The depth of this elevated dissipation increases to ≈ 70 m. After the storm, during station 11, dissipation is elevated near the surface to ≈ 20 m depth (though this may be contaminated by the ship's wake) and between 55 and 65 m depth (Figure 2b). The deeper level is coincident with the base of the storm-generated surface inertial current (Figure 2c). This suggests that the source of the deeper elevated dissipation during station 11 is shear at the base of that inertial current.

The observed vertical structure of the near-inertial shear has two salient features. First, there is a signature of the phase progressing downward with increasing time as the shear variance propagates into the upper ocean (Figure 3, top). Second, the shear vector traces an ellipse with time, indicating a slightly superinertial

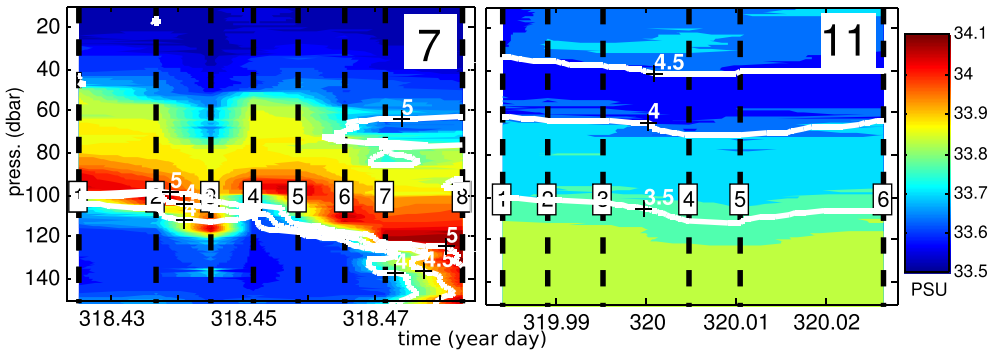

Figure 4. Contours of salinity for stations 7 and 11. The time of each microstructure profile is indicated by a numbered dashed black line. Contours of temperature in 0.5°C intervals from 3 to 5°C are shown in white.

response (Figure 3a), where the orientation of the ellipse in the horizontal, i.e., the azimuth of the major axis, varies with depth over the course of an inertial period. The shear vector alternates between elliptical and rectilinear polarizations with depth (Figure 3b). The elliptical traces have a sense of counterclockwise phase rotation with depth, and the depth-averaged shear vector executes a counterclockwise rotation with time at approximately one inertial period. As will be discussed in section 4, these features are difficult to interpret in terms of the linear kinematics of a slowly modulated wave packet. Subinertial shear, time averaged over ~1.5 inertial periods, also has the sense of counterclockwise rotation with depth (Figure 3c).

4. Discussion

There are two main features in our observations that depart from traditional views of the upper ocean response to wind forcing, as encapsulated in one-dimensional boundary layer models and the β dispersion paradigm of inertial pumping.

The first of these features is the apparent resilience of upper ocean stratification to wind forcing. For example, in station 7, near the peak of the storm, there is no appreciable mixed layer despite the occurrence of large rates of turbulent dissipation. This dissipation is coincident with a large (of order 10 m) Thorpe overturning length [*Thorpe*, 1977], which suggests that a substantial fraction of the upper ocean is actively mixing [*Brainerd and Gregg*, 1995]. The station is characterized by the presence of a sizable thermocline at ≈ 120 m (with a near-constant temperature of 5°C above this depth) and a layer of high-salinity (≈ 34 practical salinity unit) water between 90 and 100 m. At depths shallower than 100 m, stratification is maintained by a vertical gradient in salinity (Figure 4). This suggests that the lack of an observable mixed layer during station 7 may well be due to the entrainment of high-salinity water into the actively mixing upper ocean. This observed layer of high-salinity water is below the nominal depth of wind penetration (see Appendix B). However, uncertainties in the wind stress estimate and in the $O(1)$ constant relating wind stress to wind penetration depth may imply a larger depth of wind penetration. Alternatively, the entrainment of high-salinity waters may be driven by wind-generated near-inertial shear below the nominal depth of wind penetration. Unfortunately, the limited information on the horizontal structure of the ocean contained in our data set prevents us from determining the process responsible for the presence of the high-salinity layer during stations 6–8. The nearest waters with similar temperature and salinity to those of the high-salinity layer were observed later in the cruise to the south of the observation area, on the Kerguelen shelf.

Similarly, stations 9–11, occupied within hours of the end of the storm, show little evidence of a mixed layer. Rather, the vertical gradient in density within the top 50 m (the approximate mixed layer depth observed in station 8) of stations 9–11 is comparable to that in the pycnocline, below 100 m depth. In the presence of lateral density gradients, changes in upper ocean stratification can be driven through a combination of air-to-sea buoyancy flux and (sub)mesoscale frontal instabilities. During the poststorm period of the observations, the temperatures of the surface ocean and air are very close: air temperature varies between 2 and 8°C and sea surface temperature between 6.5°C and 5.5°C, indicating that no significant thermal forcing of the ocean is occurring (see Appendix C).

The upper ocean's response to wind forcing in the presence of a significant lateral density gradient (such as that associated with the ACC front where the observations were obtained) is critically dependent on the relative orientation of the wind and the frontal flow. In the absence of wind forcing, mesoscale horizontal straining leads to an intensification of the horizontal density gradient, and ageostrophic secondary circulations evolve that steepen frontal isopycnals, a process known as frontogenesis [*Hoskins and Bretherton*, 1972; *Hoskins*, 1982]; conversely, the effect of friction on the frontal flow produces ageostrophic secondary circulations that flatten frontal isopycnals, "spinning down" the front [*Garrett and Loder*, 1981]. As wind forcing ensues, a surface Ekman transport is generated. Down-front (up-front) winds drive a destratifying (restratifying) Ekman flow that steepens (flattens) frontal isopycnals [*Thomas and Lee*, 2005; *Thomas and Ferrari*, 2008], whereas cross-front winds may drive an Ekman flow either in-line (i.e., accelerating) or opposed (i.e., retarding) to the frontal flow that will, respectively, steepen or flatten isopycnals. The change in orientation of the wind as the storm passes the observation site from cross front (accelerating) to along/across (destratifying/decelerating) (Figure 2a) suggests that the occurrence of significant wind-driven restratification during or after the storm is unlikely.

Once wind forcing has ceased, initial Rossby adjustment of lateral density gradients [*Tandon and Garrett*, 1995, 1994] restratifies the upper ocean to a state where the balanced Richardson number (Ri) is reduced to $O(1)$ and mixed layer instabilities begin to develop [*Boccaletti et al.*, 2007; *Fox-Kemper and Ferrari*, 2008]. However, the bulk of the mixed layer restratification occurs only after the mixed layer instabilities reach finite amplitude, a process that occurs over a time period of greater than 1 day [*Fox-Kemper et al.*, 2008]. The rate of this restratification is suggested by numerical studies to be of the order of a fivefold increase in stratification over 6 days [*Boccaletti et al.*, 2007]. This is significantly longer than the period of the observed changes in stratification. Estimating the balanced Richardson number as $Ri = (N^2 f^2)/M^4$, where N and M are the volume-averaged vertical and horizontal buoyancy frequencies, respectively, and f is the inertial frequency [*Fox-Kemper and Ferrari*, 2008], using our observations of upper ocean vertical and horizontal density gradients and vertical gradients in horizontal velocity at the end of the storm yields Ri values in the range of 10–100 (see Appendix D). Thus, there is no evidence in our data to attribute the upper ocean changes in stratification documented here to either Rossby adjustment or to mixed layer baroclinic instabilities. However, the available information on the lateral structure of the study area is insufficient to determine the likely causes of the observed rapid changes in stratification, and a contribution from lateral (sub)mesoscale instabilities cannot be definitively ruled out.

The second prominent departure from traditional views of the upper ocean response to wind forcing found in our observations concerns both the vertical structure of the near-inertial shear and its appearance at depth only 1 day after the storm (Figure 3). The vertical structure of the near-inertial shear is at odds with linear kinematics-based expectations for a single wave packet, which should exhibit opposing directions of phase and energy propagation and a major axis with a stable azimuth. Here there is a signature of the phase progressing downward with increasing time as the shear propagates into the upper ocean (Figure 3, top), which is at odds with the inferred downward energy propagation for a wind-generated current, while the shear vector traces an ellipse with time where the azimuth of the major axis varies with depth over the course of an inertial period (Figure 3a). Given these discrepancies, the subsequent ability of the observed near-inertial shear to radiate downward is unclear. In the context of upper ocean mixing, the observed poststorm dissipations, resulting from the observed near-inertial shear (Figure 2c), are significantly above background, comparable to or larger than previously reported elevated transition layer mixing [*Sun et al.*, 2013], despite the absence of a detectable transition layer.

The β dispersion paradigm has been noted to predict accurately the decay of kinetic energy in the mixed layer [*D'Asaro*, 1989], and estimates of the spatial distribution of the decay time scale for mixed layer near-inertial oscillations using satellite-tracked drifter trajectories are in reasonable agreement with the predictions of such linear radiation theory [*Park et al.*, 2009]. However, it has also been demonstrated that the β dispersion model fails to capture fully all observations of the evolution of near-inertial currents; most significantly the model fails at small scales in reproducing observations of the evolution of near-inertial shear [*D'Asaro*, 1995; *Dohan and Davis*, 2011].

Variation in the background relative vorticity changes the effective inertial frequency experienced by the near-inertial currents, which in regions of anticyclonic relative vorticity increase the width of the internal wave frequency range [*Kunze*, 1985] and relative vorticities of order $0.3f$ associated with strong upper ocean

fronts have been observed to influence both the horizontal scale and structure of near-inertial currents [*Lee and Eriksen*, 1997]. Local gradients of relative vorticity also modulate β, causing a reduction in the scales of inertial motion and accelerating their downward propagation [*Van Meurs*, 1998; *Danioux et al.*, 2008, 2011].

Following *Elipot et al.* [2010] and estimating mesoscale relative vorticity for the observation site from AVISO sea surface current data (using the revised post-2014 data set) gives an average relative vorticity that is cyclonic, consistent with the relative position of the observation site to the front, with magnitude $3 \pm 0.3 \times 10^{-6}\ s^{-1} \approx 0.03f$ for the period of the observations. This is of similar magnitude ($0.02f$) to that observed during the Ocean Storms Experiment [*D'Asaro*, 1995]. The gradient in relative vorticity for the same time period is also small ($5 \pm 2 \times 10^{-11}\ s^{-1}\ m^{-1}$) of the same order as β. An approximate timescale (t_1) for the decay of the near-inertial current can be estimated from the time for the first baroclinic mode to become 90° out of phase [*Gill*, 1984]. Using

$$t_1^{\,3} = \frac{3\pi}{f\nabla\zeta.\nabla\zeta R_1^{\,2}}$$

[*Van Meurs*, 1998], where $\nabla\zeta$ is the gradient in relative vorticity, and with a typical value of 3×10^4 m for the R_1, the Rossby radius of the first baroclinic mode, returns a timescale ≈ 4 days, which is comparable to the timescale calculated using $\beta = 1.6 \times 10^{-11}\ s^{-1}m^{-1}$ of 8.4 days.

While this suggests that the apparent rapid evolution of the observed near-inertial current is unlikely to be due to the effect of mesoscale relative vorticity, the coarse resolution of the AVISO data does not rule out the presence of localized small-scale fronts which may have significantly higher relative vorticity. It has also been suggested that such small-scale fronts may act to scatter near-inertial motions, converting them to higher-frequency waves, or that the inertial motions may interact directly with the internal wave field through nonlinear interactions [*D'Asaro*, 1995]. However, as discussed above, the balanced Richardson number estimated for the poststorm period (Appendix D) is consistently much greater than unity, suggesting that the presence of such small-scale upper ocean fronts is not a robust feature of these data.

5. Conclusions

The observations presented here of the passage of a short, intense storm in close proximity to an ACC front reveal the evolution of near-inertial shear in stratified upper ocean waters on a surprisingly short time scale (approximately 1 day). The subsequent ability of the near-inertial motions to radiate downward and contribute to the maintenance of the ocean's general circulation is unclear, since the temporal evolution and vertical structure of those motions are not readily interpretable in terms of the linear kinematics of a single plane wave. However, this near-inertial shear is observed to drive upper ocean mixing of magnitude comparable to or larger than previously reported enhanced transition layer mixing [*Sun et al.*, 2013].

Key to this behavior is the observed resilience of upper ocean stratification to wind forcing and, in particular, the observed changes in stratification of the near-surface ocean within a day of the end of the storm. The causes of these rapid changes in stratification cannot be ascertained with our data. The limited available information on the lateral structure of the study area and its proximity to an ACC front suggest that spatially nonlocal processes involving differential horizontal advection (such as (sub)mesoscale instabilities) cannot be definitively ruled out. We note that the lateral scale of the storm is both significantly larger than the area of the observations site and also greater than the largest plausible lateral excursions of water parcels in the vicinity of the observation site for the period of data acquisition. As such, all measured upper ocean waters are likely to have experienced similar atmospheric forcing, so that the observed changes in upper ocean stratification documented here are the plausible result of active ocean dynamics rather than passive advection of a spatially inhomogeneous near-surface density field.

In conclusion, our study documents the evolution of near-inertial shear in stratified upper ocean waters that is seemingly at odds with existing views of the surface ocean response to wind forcing. Given the disproportionately important role that intense storm events are suggested to play in the generation of the near-inertial wavefield that pervades the global ocean interior [*Plueddemann and Farrar*, 2006], further research into the phenomenology of storm forcing of upper ocean fronts is called for.

Appendix A: Extracting Inertial Signal From ADCP Data by Band-Pass Filtering

The width and shape of the filter window were empirically determined to best extract the inertial component from a synthetic data set of the same temporal resolution as the ADCP data, consisting of two sine curves of equal power (one at the local inertial frequency and one at the M2 tidal frequency) contaminated with random zero mean noise. In order to minimize the effect of the filter transfer function, observable when filtering the synthetic data set within approximately 1.6 days of the record ends, mirror boundary conditions were applied. The filter was then applied to the padded ADCP data and the middle third of the output, corresponding to the original ADCP data, extracted.

Appendix B: Depth of Wind Penetration

We estimate the depth of wind penetration (D_{Ek}) from the scaling

$$D_{Ek} \propto u^*(Nf)^{-1/2}$$

[*Large et al.*, 1994], where $u^* = \sqrt{|\tau|/\rho}$ is the friction velocity, f the local Coriolis frequency, ρ the surface ocean density, τ the wind stress, and N the buoyancy frequency. Assuming a constant of proportionality of order 1, D_{Ek} is estimated from the observations as $\approx$ 15 m for station 6, and as $\approx$ 50 m for station 7, consistent with the observed mixed layer depths for stations 6 (prestorm $\approx$11 m) and 8 (poststorm $\approx$ 48 m). The observed vertical profile of the dissipation rate indicates that there is turbulent mixing occurring below this estimated maximum depth of wind penetration (Figure 2).

Appendix C: Air-Sea Buoyancy Fluxes

Air temperature during the period of the measurements varies between 2 and 8°C. Prior to the storm, the air temperature is between 4 and 5°C. The onset of the storm is accompanied by an increase in air temperature of $\approx$ 3°C, with air temperature dropping to $\approx$ 2°C briefly after the storm before recovering back to 4°C by year day 319. The passage of the storm results in a 1°C drop in the sea surface temperature, from $\approx$ 6.5°C to $\approx$ 5.5°C.

Estimating the bulk sensible heat flux from shipboard observations using the method of *Fairall et al.* [1996] gives an average sensible heat flux (Q_s) of 12.6 W m^{-2} out of the ocean for the period of the observations. The corresponding buoyancy flux B_s calculated using

$$B_s = \frac{g\alpha Q_s}{\rho C_w}$$

[*Gill*, 1982], where α and C_w are the thermal expansion coefficient and specific heat capacity for seawater, respectively, and ρ, a reference density, is 3.8×10^{-9} W kg^{-1} (4×10^{-3} mW m^{-2} converted using the mean surface density from station 11 of 1026.9 kg m^{-3}). This indicates that the total air-sea buoyancy fluxes are likely to have negligible impact on the structure of the mixed layer.

Appendix D: Estimating the Balanced Richardson Number

During the period of the observations, vertical shear, calculated from 150 kHz ADCP and averaged into inertial periods, is of order 5×10^{-4} s^{-1}, which is consistent with a horizontal density gradient of order 5×10^{-6} kg m^{-4} for a front in thermal wind balance.

The region was subsequently reoccupied and systematically surveyed from 2 to 8 December 2008. Upper ocean (averaged over the uppermost 100 m) horizontal density gradients estimated using the CTD section data from this later occupation are 3.4×10^{-6} kg m^{-4} between stations bracketing the site of the observations. Vertical geostrophic shears, estimated from the CTD section, are in the range of $1–8 \times 10^{-4}$ s^{-1}, consistent with thermal wind balance for a cross-front horizontal density gradient of $1–8 \times 10^{-6}$ kg m^{-4}. Note, however, that we do not mean to imply that the details of upper ocean stratification are stationary between the two occupations.

The balanced Richardson number is expressed as

$$Ri = (N^2 f^2)/M^4$$

where N and M are the volume-averaged vertical and horizontal buoyancy frequencies, respectively, and f is the inertial frequency [*Fox-Kemper and Ferrari*, 2008]. Using $M^2 = 5\times10^{-8}$ s^{-1} estimated from a horizontal density gradient of 5×10^{-6} kg m^{-4} and the average buoyancy over the top 100 m depth for stations 8–10 ($N^2 = 1.75 \times 10^{-5}$ s^{-1}) gives a balanced Richardson number of order 80 for these observations.

The balanced Richardson number was also calculated using

$$Ri = \frac{N^2}{S_g{}^2}$$

[*Fox-Kemper and Ferrari*, 2008], where $S_g{}^2$ is the geostrophic shear. Using the time mean shear estimated from the 150 kHz ADCP data over the time period 12 h either side of each station as an approximation to the geostrophic shear, the Richardson number is never less than order 10.

Acknowledgments

The authors wish to thank the officers, crew, and entire scientific compliment aboard the RRS *James Cook* during cruise JC29. The SOFine project is funded by the UK Natural Environmental Research Council (NERC) (grant NE/G001510/1). The data used in the preparation of this manuscript are available on request from The British Oceanographic Data Centre (http://www.bodc.ac.uk).

The Editor thanks two anonymous reviewers for their assistance in evaluating this paper.

References

Boccaletti, G., R. Ferrari, and B. Fox-Kemper (2007), Mixed layer instabilities and restratification, *J. Phys. Oceanogr.*, *37*, 2228–2250.

Brainerd, K. E., and M. C. Gregg (1995), Surface mixed and mixing layer depths, *Deep Sea Res., Part I*, *42*(9), 1521–1543.

Danioux, E., P. Klein, and P. Rivière (2008), Propagation of wind energy into the deep ocean through a fully turbulent mesoscale eddy field, *J. Phys. Oceanogr.*, *38*, 2224–2241, doi:10.1175/2008JPO3821.1.

Danioux, E., P. Klein, M. Hecht, N. Komori, G. Roullet, and S. Le Gentil (2011), Emergence of wind-driven near-inertial waves in the deep ocean triggered by small-scale eddy vorticity structures, *J. Phys. Oceanogr.*, *41*, 1297–1307.

D'Asaro, E. (1985), The energy flux from the wind to near-inertial motions in the surface mixed layer, *J. Phys. Oceanogr.*, *15*(8), 1043–1059.

D'Asaro, E. (1989), The decay of wind-forced mixed layer inertial oscillations due to the β-effect, *J. Geophys. Res.*, *94*(C2), 2045–2056.

D'Asaro, E. A. (1995), Upper-ocean inertial currents forced by a stromg storm. Part II: Modeling, *J. Phys. Oceanogr.*, *25*(11), 2937–2952.

Dee, D. P., et al. (2011), The ERA-Interim reanalysis: Configuration and performance of the data assimilation system, *Q. J. R. Meteorol. Soc.*, *137*(656), 553–597, doi:10.1002/qj.828.

Dohan, K., and R. E. Davis (2011), Mixing in the transition layer during two storm events, *J. Phys. Oceanogr.*, *41*(1), 42–66, doi:10.1175/2010JPO4253.1.

Elipot, S., R. Lumpkin, and G. Prieto (2010), Modification of inertial oscillations by the mesoscale eddy field, *J. Geophys. Res.*, *115*, C09010, doi:10.1029/2009JC005679.

Fairall, C. W., E. F. Bradley, D. P. Rogers, J. B. Edson, and G. S. Young (1996), Bulk parameterization of air-sea fluxes for tropical ocean-global atmosphere coupled-ocean atmosphere response experiment, *J. Geophys. Res.*, *101*(C2), 3747–3764, doi:10.1029/95JC03205.

Ferrari, R., and C. Wunch (2009), Ocean circulations kinetic energy: Reservoirs, sources and sinks, *Annu. Rev. Fluid Mech.*, *41*, 253–282.

Fox-Kemper, B., and R. Ferrari (2008), Parameterization of mixed layer eddies. Part II: Prognosis and impact, *J. Phys. Oceanogr.*, *38*(6), 1166–1179.

Fox-Kemper, B., R. Ferrari, and R. Hallberg (2008), Parameterization of mixed layer eddies. Part I: Theory and diagnosis, *J. Phys. Oceanogr.*, *38*(6), 1145–1165.

Garrett, C., and J. Loder (1981), Dynamical aspects of shallow sea fronts, *Philos. Trans. R. Soc. London, Ser. A*, *302*(1472), 563–581.

Gill, A. (1982), *Atmosphere-Ocean Dynamics*, Academic Press, London.

Gill, A. (1984), On the behavior of internal waves in the wakes of storms, *J. Phys. Oceanogr.*, *14*(7), 1129–1151.

Hoskins, B. (1982), The mathematical theory of frontogenesis, *Annu. Rev. Fluid Mech.*, *14*(1), 131–151.

Hoskins, B., and F. Bretherton (1972), Atmospheric frontogenesis models: Mathematical formulation and solution, *J. Atmos. Sci.*, *29*, 11–37.

Johnston, T. M. S., and D. L. Rudnick (2009), Observations of the transition layer, *J. Phys. Oceanogr.*, *39*(3), 780–797, doi:10.1175/2008JPO3824.1.

Kara, A., P. Rochford, and H. Hurlburt (2000), An optimal definition for ocean mixed layer depth, *J. Geophys. Res.*, *105*(C7), 16,803–16,821.

Kunze, E. (1985), Near-inertial wave propagation in geostrophic shear, *J. Phys. Oceanogr.*, *15*(10), 554–656.

Large, W., J. McWilliams, and S. Doney (1994), Oceanic vertical mixing—A review and a model with a nonlocal boundary-layer parameterization, *Rev. Geophys.*, *32*(4), 363–403.

Lee, C. M., and C. C. Eriksen (1997), Near-inertial internal wave interactions with mesoscale fronts: Observations and models, *J. Geophys. Res.*, *102*(C2), 3237–3253.

Moum, J., M. Gregg, R. Lien, and M. Carr (1995), Comparison of turbulence kinetic-energy dissipation rate estimates from two ocean microstructure profilers, *J. Atmos. Oceanic Technol.*, *12*(2), 346–366.

Naveira Garabato, A. (2009), Cruise report, no. 35 *RRS James Cook* cruise 29 01 Nov-22 dec 2008 SOFine Cruise Report: Southern ocean finestructure, *Tech. Rep.*, Univ. of Southampton, Southampton, U. K.

Park, J., K. Kim, and R. Schmitt (2009), Global distribution of the decay timescale of mixed layer inertial motions observed by satellite-tracked drifters, *J. Geophys. Res.*, *114*, C11010, doi:10.1029/2008JC005216.

Plueddemann, A., and J. Farrar (2006), Observations and models of the energy flux from the wind to mixed-layer inertial currents, *Deep Sea Res., Part II*, *53*, 5–30, doi:10.1016/j.dsr2.2005.10.017.

Pollard, R., and R. Millard Jr. (1970), Comparison between observed and simulated wind-generated inertial oscillations, *Deep Sea Res., Oceanogr. Abstr.*, *17*(4), 813–816, doi:10.1016/0011-7471(70)90043-4.

Prandke, H. (2007), Correction of the spatial response of shear sensors in dissipation rate computation procedure, *Tech. Rep.*, ISW Wassermesstechnik, Petersdorf.

Price, J., R. Weller, and R. Pinkel (1986), Diurnal cycling: Observations and models of the upper ocean response to diurnal heating, cooling, and wind mixing, *J. Geophys. Res.*, *91*(C7), 8411–8427.

Rippeth, T., J. Simpson, E. Williams, and M. Inall (2003), Measurement of the rates of production and dissipation of turbulent kinetic energy in an energetic tidal flow: Red Wharf Bay revisited, *J. Phys. Oceanogr.*, *33*(9), 1889–1901.

Roget, E., I. Lozovatsky, X. Sanchez, and M. Figueroa (2006), Microstructure measurements in natural waters: Methodology and applications, *Prog. Oceanogr.*, *70*(2-4), 126–148.

Stips, A. (2005), Dissipation measurement, in *Marine Turbulence: Theories, Observations, and Models. Results of the CARTUM Project*, edited by H. Baumert, J. Simpson, and J. Sundermann, pp. 115–126, Cambridge Univ. Press, Cambridge, U. K.

Sun, O. M., S. R. Jayne, K. L. Polzin, B. A. Rahter, and L. C. St. Laurent (2013), Scaling turbulent dissipation in the transition layer, *J. Phys. Oceanogr.*, *43*, 2475–2489, doi:10.1175/JPO-D-13-057.1.

Tandon, A., and C. Garrett (1994), Mixed layer restratification due to a horizontal density gradient, *J. Phys. Oceanogr.*, *24*, 1419–1424.

Tandon, A., and C. Garrett (1995), Geostrophic adjustment and restratification of a mixed layer with horizontal gradients above a startified layer, *J. Phys. Oceanogr.*, *25*, 2229–2241.

Thomas, L., and R. Ferrari (2008), Friction, frontogenesis, and the stratification of the surface mixed layer, *J. Phys. Oceanogr.*, *38*, 2501–2518, doi:10.1175/2008JPO3797.1.

Thomas, L., and C. Lee (2005), Intensification of ocean fronts by down-front winds, *J. Phys. Oceanogr.*, *35*, 1086–1102.

Thorpe, S. (1977), Turbulence and mixing in a Scottish loch, *Philos. Trans. R. Soc. London, Ser. A*, *286*(1334), 125–181.

Van Meurs, P. (1998), Interactions between near-inertial mixed layer currents and the mesoscale: The importance of spatial variabilities in the vorticity field, *J. Phys. Oceanogr.*, *28*(7), 1363–1388.

Welch, P. (1967), The use of fast Fourier transform for the estimation of power spectra: A method based on time averaging over short, modified periodograms, *IEEE Trans. Audio Electroacoust.*, *AU15*(2), 70–73.

Wunch, C., and R. Ferrari (2004), Vertical mixing energy and the general circulation of the oceans, *Annu. Rev. Fluid Mech.*, *36*, 281–314.

Yamazaki, H., and T. Osborn (1990), Dissipation estimates for stratified turbulence, *J. Geophys. Res.*, *95*(C6), 9739–9744.